Journal of the European Ceramic Society 43 (2023) 5871–5881

Contents lists available at ScienceDirect

Journal of the European Ceramic Society

journal homepage: www.elsevier.com/locate/jeurceramsoc

Powder bed fusion of polyamide powders combined with different preceramic polymers infiltration and pyrolysis to produce complex-shaped ceramics

Marco Pelanconi [a,b,*], Samuele Bottacin [a], Paolo Colombo [b,c], Alberto Ortona [a]

[a] University of Applied Sciences (SUPSI): Mechanical Engineering and Materials Technology Institute (MEMTi), Polo Universitario Lugano, 6962 Lugano, Switzerland
[b] Department of Industrial Engineering, University of Padova, 35131 Padova, Italy
[c] Department of Materials Science and Engineering, The Pennsylvania State University, University Park, PA 16802, USA

ARTICLE INFO

Keywords:
Powder bed fusion
Infiltration
Preceramic polymers
TPMS
Polymer derived ceramics

ABSTRACT

The fabrication of a wide range of polymer-derived ceramic parts with high geometric complexity through a novel hybrid additive manufacturing technique is presented in this article. The process that we introduced in a previous work uses the powder bed fusion technology to manufacture high porous polymeric preforms to be then converted into ceramics through preceramic polymer infiltration and pyrolysis. The cellular architectures of a rotated cube (strut-based) and a gyroid (sheet-based) with 25 mm diameter, 44 mm height and 67 % of geometric macroporosity were generated and used for the fabrication. The complex structures were 3D printed and polycarbosilane, polycarbosiloxane, polysilazane and furan liquid polymers were used to produce SiC, SiOC, SiCN and glassy carbon, respectively. Despite a linear shrinkage of about 24 %, the parts maintained their designed complex shape without deformations. The significant advantages of the proposed method are the maturity of powder bed fusion for polymers with respect to ceramic additive manufacturing techniques and the possibility to fabricate net-shape complex ceramic parts directly from preceramic precursors.

1. Introduction

In recent years, the development of advanced ceramics for high temperature applications has experienced significant growth, thanks to their use in the aerospace, military and defense, energy management industries, automotive, biotechnology, communication, and chemical processing. Advanced ceramic components with stringent specifications are manufactured from highly refined raw materials, providing unique or superior functional attributes [1–5]. This class of materials offers unmatched properties that cannot be provided by metals, especially when considering non-oxide ceramics. For this reason, they are used for the design of components operating at temperature higher than 1000 °C, such as heat exchangers, solar absorbers, industrial burners, energy plants and heat storage systems [6–8].

A significant opportunity for manufacturing advanced ceramic materials is represented by additive manufacturing (AM) [9,10]. Compared to the conventional production processes, AM of ceramics offers several technological advantages [11–13], such as high-efficiency, rapid manufacturing processes, fabrication of geometrically-complex parts, net-shape components produced without the need of additional machining and avoiding secondary processing, shortening of development cycle, cost reduction, and unique properties due the use of highly engineered design [14–17]. Nowadays, AM of ceramics is leading to the opening of new application areas and to new generation components, such as catalysts, adsorbers, porous burners and reactors, heat dissipator and high temperature heat exchangers [18–23]. However, great progress has been made to date for the additive manufacturing of oxide ceramics [24–30] and less so for the additive manufacturing of non-oxide ceramics [31–33].

At present, almost all AM-based non-oxide ceramics are produced through a multi-steps procedure, due to the high sintering temperature of these materials. The process comprises two steps: (i) the preparation of the ceramic preform through different 3D printing methods, and (ii) the densification of the preform through several strategies, including polymer impregnation and pyrolysis (PIP), liquid silicon infiltration (LSI), chemical vapor infiltration (CVI), chemical vapor deposition

* Corresponding author at: University of Applied Sciences (SUPSI): Mechanical Engineering and Materials Technology Institute (MEMTi), Polo Universitario Lugano, 6962 Lugano, Switzerland.
E-mail address: marco.pelanconi@supsi.ch (M. Pelanconi).

https://doi.org/10.1016/j.jeurceramsoc.2023.06.053
Received 19 April 2023; Received in revised form 5 June 2023; Accepted 18 June 2023
Available online 20 June 2023

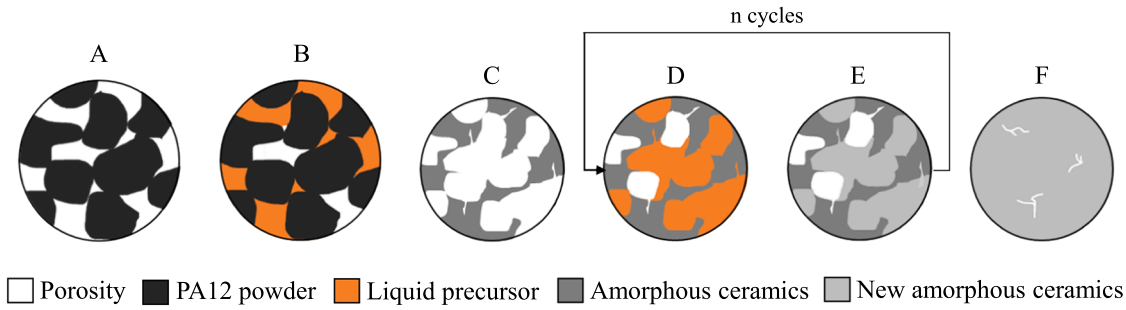

Fig. 1. Scheme of the process principle: (A) powder bed fusion of the porous preform; (B) liquid precursor infiltration; (C) pyrolysis; (D) additional infiltration; (E) additional pyrolysis; (F) dense ceramic sample.

(CVD), cold isostatic pressing (CIP) and hot isostatic pressing (HIP) [34–43]. An interesting approach has been proposed using preceramic polymers [44] as alternative to the elaborate processing of ceramic powders. Preceramic polymers, or ceramic precursors, are polymeric compounds that are converted into ceramics through pyrolysis (800–1100 °C) in an oxygen-free environment [15,44–48]. The ceramics produced are called polymer derived ceramics (PDCs) and can be used directly in the 3D printing [49,50,59,60,51–58] or in the infiltration process [61–65] for the densification of the material.

However, not all these techniques allow for the production of complex geometries, such as lattice and triply periodic minimal surface (TPMS) structures [66–68]. The main problems are related to the weak resolution of the ceramic AM technologies and to several problems with the processing of ceramics. For example, stereolithography allows to reach high resolution but high powder packing isn't possible because of the powder's opacity and therefore leading to high porous and fragile parts. The replica process instead does not allow to reach high resolution and the production of complex parts is not allowed. Powder-based techniques have the difficulty to remove the unbound powder, especially when geometric complex parts are manufactured and the green part is very fragile. A 3D highly detailed structure cannot be produced with filament extrusion techniques at present due to a lack of geometric freedom. Therefore, not all the ceramic AM techniques are best suited to produce complex ceramic architectures.

In this work, we used our novel hybrid AM approach [69] for the fabrication of a wide range of polymer-derived ceramic parts. The process exploits the powder bed fusion of geometrically complex architectures with controlled microporosity made by polyamide. The preforms are then converted into ceramics by preceramic polymer infiltration and pyrolysis. The process is very flexible in reference to the material to be produced. In this study polycarbosilane, polycarbosiloxane, polysilazane and furan liquid polymers were used for the fabrication of lattice and TPMS structures made by SiC, SiOC, SiCN and C respectively.

2. Materials and methods

The previously introduced hybrid approach [69] exploits the 3D printing of polymer powders combined with precursor infiltration and pyrolysis. The process involves the use of powder bed fusion technology for the preparation of a polyamide preform with high microporosity, essential to achieve a subsequent infiltration using a liquid preceramic polymer and therefore a more effective conversion into ceramics. Pyrolysis at 1000 °C is then used to obtain the polymer-derived ceramic, and only a few PIP cycles are used for the final densification of the part. The process principle is illustrated in Fig. 1.

2.1. Design of the complex architectures

Complex structures were designed through purpose-built algorithms developed at SUPSI. The computational design tools were developed in Grasshopper using the Rhinoceros software for the visualization

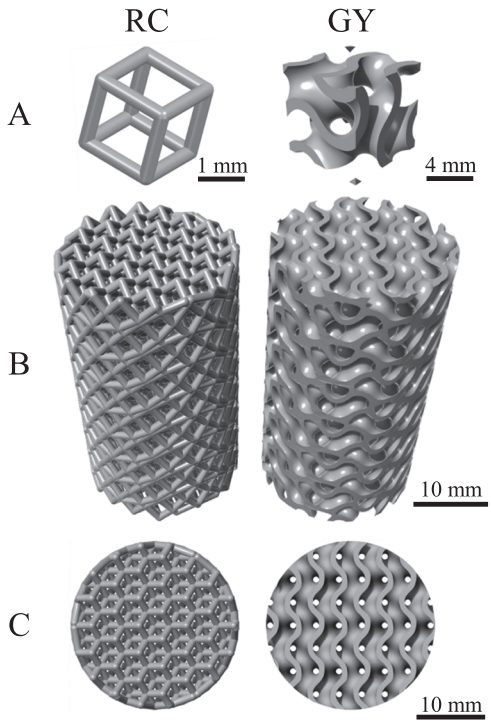

Fig. 2. Computational models of the rotated cube (RC) and gyroid (GY) architectures: (A) unit cells; (B) cylindrical structures; (C) frontal views.

(McNeel, Seattle, Washington, USA). Two topologies were investigated in this work, namely a Rotated Cube (RC) and a Gyroid (GY). The first is a lattice-based structure made by struts arrangement and comprised with cubic unitary cells, rotated 45 ° on each axis. The second is a TPMS-based structure made by a continuous arrangement of surfaces and designed by plotting the approximation of the mathematical function of

Table 1
Geometric properties of the two designed cylindrical models: rotated cube (RC) and gyroid (GY).

Architecture type	–	RC	GY
Unit cell type (C_t)	dimensionless	Rotated cube	Gyroid
Unit cell size (C_S)	mm	2.9	6.8
Struts diameter or surface thickness (t)	mm	1.1	1.0
Sample diameter (D)	mm	25.0	25.0
Sample height (H)	mm	44.0	44.0
Geometric surface area (GSA)	cm^2	204.9	203.0
Solid volume (V_s)	cm^3	7.1	7.2
Total volume occupied (V_{tot})	cm^3	21.5	21.5
Specific geometric surface area ($SGSA$)	1/m	950.8	942.3
Geometric (macro) porosity (φ_M)	%	67	67

Table 2
Preceramic polymers used for the fabrication of different polymer-derived ceramics.

AHPCS	Full name:	Allylhydridopolycarbosilane
	Commercial name:	StarPCS™ SMP-10
	Supplier:	Starfire Systems Inc, NY, USA
	Polymer-derived ceramic:	Silicon Carbide (SiC)
PCSO	Full name:	Polycarbosiloxane
	Commercial name:	MS-154
	Supplier:	EEMS-LLC, NY, USA
	Catalyst added:	CLC-PB055 (EEMS-LLC, NY, USA) 1 %wt
	Polymer-derived ceramic:	Silicon Oxycarbide (SiOC)
PSN	Full name:	Polysilazane
	Commercial name:	Durazane 1800
	Supplier:	Merck KgaA, Darmstad, DE
	Polymer-derived ceramic:	Silicon Carbonitride (SiCN)
FUR	Full name:	Furanic resin (or carbon thermosetting resin)
	Commercial name:	Furolite 100
	Supplier:	TransFurans Chemicals, Geel, BE
	Catalyst added:	HM 1448 (WIZ chemicals, Dairago, IT) 5 %wt
	Polymer-derived ceramic:	Glassy carbon (C)

the gyroid (Eq. 1).

$$GY = \sin x \bullet \cos y + \sin y \bullet \cos z \bullet \sin z \bullet \cos x \quad (1)$$

The two structures were generated by maintaining the same geometric characteristics, such as the amount of geometric surface area and the geometric porosity (or macroporosity). This was achieved by using two different unit-cell sizes (C_s) and thickness of the struts or surface (t). The architectures construction takes place from the single unit cell (Fig. 2A) that is three-dimensionally patterned to the desired cylindrical form with a diameter (D) of 25 mm and length (H) of 44 mm. Table 1 summarizes the geometric properties of the two structures, Fig. 2B shows their 3D computational models and Fig. 2C shows the frontal view of the structures.

2.2. Manufacturing

2.2.1. Materials

Polyamide 12 powders (d50: 60 μm) (PA12, Sintratec AG, Brugg, Switzerland) were used for the powder bed fusion 3D printing. PA12 is a thermoplastic material with the formula [-(CH2)11 C(O)NH-]$_n$ and a density of 1.0 g/cm^3.

Table 2 shows the four different liquid preceramic polymers used for the infiltration of the 3D printed preforms. All these polymers are solvent-free.

The addition of the catalysts was needed to promote the crosslinking of the preceramic polymers before the complete melting of the PA12 preform, and to maintain the pristine shape of the sample. Preceramic polymers used without catalyst were able to thermal crosslink during processing. A planetary centrifugal mixer (Thinky Mixer ARE-250, Thinky, USA) was used to mix the preceramic polymer with its catalyst at 700 rpm for 3 min. All the preceramic polymers have about the same density of 1.0 g/cm^3 and dynamic viscosity of 40–100 cPs at 25 °C.

2.2.2. 3D printing of the complex architectures

The manufacturing of the polymeric preform was performed in air using a commercially available powder bed fusion 3D printer (Sintratec KIT, Sintratec AG, Brugg, Switzerland) with a low-power laser beam driven by motorized mirrors (laser wavelength blue: 445 nm, diode laser power: 2.3 W, spot size: 250 μm, max laser speed: 1000 mm/s, speed in z: 11 mm/h, in-plane resolution ≈ 250 μm). The complex-shaped design models were 3D printed by using the following printing parameters: laser speed of 848 mm/s, layer thickness of 100 μm and powder surface temperature of 166 °C. This combination allows to obtain parts with high porosity, essential for the subsequent infiltration [69,70].

2.2.3. Preceramic polymer infiltration and pyrolysis

The 3D printed complex structures were infiltrated with the selected liquid precursors in light vacuum (~10^{-1} bar) at room temperature with a purpose-built apparatus. The parts were placed one by one in a chamber, and once the vacuum was pulled by a pump, they were immersed in the liquid preceramic polymer for one minute. At the end, the chamber was returned to atmospheric pressure and the pieces were re-emerged. The samples after infiltrations with PCSO, PSN and FUR underwent a pre-cure treatment in a static furnace at 145 °C for 2 h before pyrolysis. This step was found to be crucial to promote the crosslinking of the preceramic polymer, and to maintain the shape of the part after pyrolysis.

After each infiltration, the samples were pyrolyzed in high purity flowing Argon (99.99 %, 30 L/h) using a vertical retort furnace (SPS01, Keos Srl, Concorezzo, IT) at the temperature of 960 °C for 1 h. A detailed description of the thermal cycle is provided in our previous work [69].

Three additional infiltration and pyrolysis cycles were performed for the sample densification, except for the carbon parts (FUR as preceramic polymer) which underwent one less cycle, due to the clogging of the lattice cells.

2.3. Characterization

The thermal behavior of the preceramic polymers was evaluated by Thermogravimetry (TGA) analysis using a thermal equipment (TGA/DSC 3 +, Mettler-Toledo GmbH, Greifensee, Switzerland). STARe software package (Thermal Analysis Software, Mettler- Toledo GmbH, Greifensee, Switzerland) was used to record the data during the analyses. Tests were performed up to 1000 °C in flowing Argon (50 mL/min) with a heating rate of 10 °C/min. PCSO, PSN and FUR were tested after the pre-curing treatment. AHPCS was tested as produced by the supplier.

During the process steps, the mass variation was recorded with a precision balance (0.1 mg resolution) and the sample size was measured using a digital caliper. These operations were performed after the 3D printing and after each PIP to investigate the weight change and the shrinkage of the parts.

Helium pycnometry (Ultrapyc3000, Anton Paar QuantaTec Inc., Florida, USA) was used to assess the density of the materials after 3D printing and PIP. The true density and the apparent density were obtained by using a bulk sample piece and sample powder. Eight tests were performed for each sample with a pressure target of 18 psi.

The phase assemblage of the ceramic parts after PIP was examined on sample powder, using an X-ray diffractometer (D8 Advance, Bruker Italia Srl, Milano, IT) with Cu(Kα) radiation, from 10° to 80°, 0.05°/step, 2 s/step. The Match! Software package (Crystal Impact GbR, Bonn, Germany) was employed for a semi-automatic phase identification, supported by data from the PDF-2 database (ICDD-International Centre for Diffraction Data, Newtown Square, PA, USA).

The microstructure of the samples was investigated through scanning electron microscopy (SEM) analyses (JSM-6010PLUS/LA, Jeol Ltd., Japan). Before the analyses, the samples were fractured and incorporated using phenolic resin.

The porosity, the pore size distribution and volume were evaluated by mercury intrusion porosimetry (MIP) tests (PoreMaster 60, Anton Paar Switzerland AG, Buchs, Switzerland) with a pressure range from 0.0014 MPa to 414 MPa. Samples after the last PIP cycle were analyzed.

Uniaxial quasi-static compression experiments were carried out to assess the mechanical strength of the samples (Zwick Z050, Zwick GmbH & Co.KG, Ulm, Germany). A constant strain rate of 10^{-3} s^{-1} was used and the force was measured with a cell load of 50 kN (KAP-S, AST, Dresden, Germany). A cylindrical sample was placed at the center of the plates and pre-loaded with a force of 5 N. Ten samples were tested for each type. Before testing, the top and bottom surfaces of the cylinders

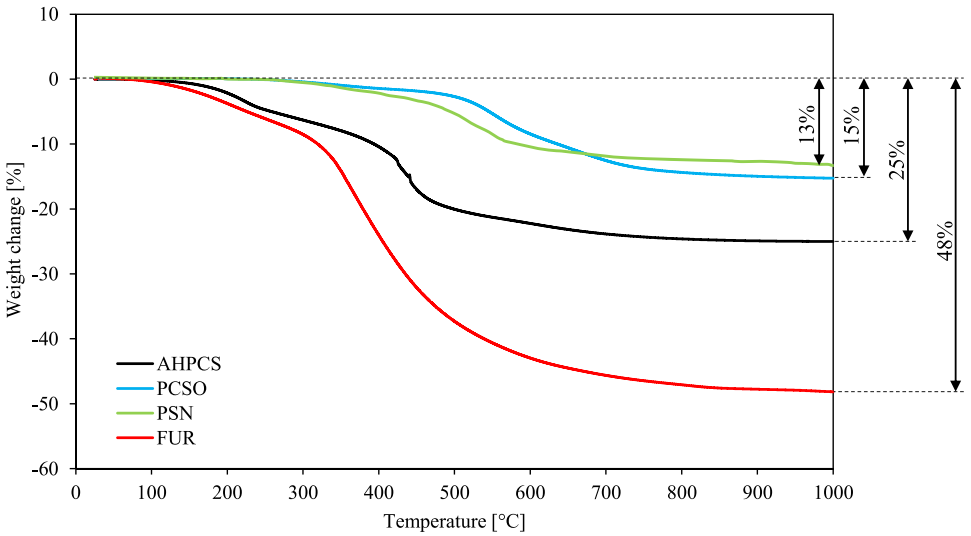

Fig. 3. TGA analysis of the four preceramic polymers in Argon up to 1000 °C: SiC precursor (AHPCS, black curve), SiOC precursor (PCSO, blue curve), SiCN precursor (PSN, green curve) and C precursor (FUR, red curve).

were lightly machined for flattening.

3. Results and discussion

3.1. Thermal behavior of the preceramic polymers

Fig. 3 shows the TGA data recorded for the four preceramic polymers in Argon. The polymers showed three different behaviors. PCSO and PSN had about the same trend: up to 200 °C no weight loss was observed due to the pre-curing treatment that provided stability to the material. A negligible weight loss was observed during the complete crosslinking of the polymers up to 350 °C. Then, the polymer-to-ceramic conversion produced a higher weight loss for PSN up to 650 °C. After this temperature an opposite behavior was observed with an increase of the weight loss for the PCSO. At 1000 °C, the final ceramic residues of the SiOC and SiCN were 85 % and 87 % respectively. According to literature [71], the pre-crosslinking of the PSN produced a higher yield with respect to the not crosslinked one (10–15 % lower) [72]. AHPCS (black curve) showed the cross-linking of the polymer between 100 and 400 °C with 10 % weight loss due to the release of oligomers. Above 400 °C an additional 15 % weight loss indicated the polymer-to-ceramic transformation. The final SiC residue was 75 % at 1000 °C. FUR showed a difference behavior despite being pre-cured similarly to PCSO and PSN. A 10 % weight loss was observed between 150 and 300 °C due to the complete crosslinking of the polymer. Then, the transformation into amorphous carbon produced an additional weight loss of about 38 %, with a final C residue of 52 %. All yields obtained agreed with the literature [60, 72–74].

3.2. Preform processing

The combination of the printing parameters allowed to 3D print the complex architectures with a relative density of 0.56 ± 0.04 and very high quality, and the samples were easy to handle and to clean despite the complicated geometry. The same combination of parameters allowed to reach a relative density of 0.52 (< 4 %) when printing discs [69,70]. This means that the cross-section size has an influence on the microporosity of the part. This can be attributed to the path of the laser beam during the 3D printing. With samples possessing a small overall thickness, the laser passes more rapidly near the just melted powder, supplying further energy in a short time, which results in an over melting of the previous path, and therefore a lower amount of micropores. Conversely, when samples have a larger thickness, the laser takes longer to pass near the just fused areas, and it does not influence the melting of the previous path.

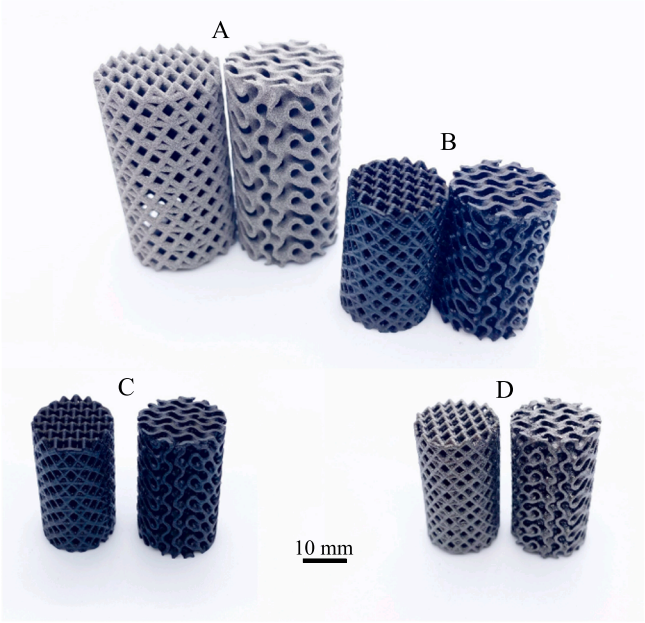

Fig. 4. Optical images of the architectures before and after PIP: (A) 3D printed structures; (B) SiC structures; (C) SiOC and SiCN structures; (D) C structures.

In accordance with the computational models, the final PA12 preforms had a diameter of 25 ± 0.47 mm, a height of 45 ± 0.64 mm and a mass of 4 ± 0.43 g. The measured struts diameter of the RC structures was 1.1 ± 0.018 mm, and the surface thickness of the GY structures was 1.0 ± 0.015 mm. Fig. 4A shows the 3D printed polymeric parts.

The 3D printed architectures were infiltrated with the selected preceramic polymers, and then pyrolyzed to produce their respective ceramic materials. The AHPCS, PCSO, PSN and FUR preceramic polymers are precursors for the following ceramic materials: SiC, SiOC, SiCN and C respectively. A small amount of oxygen is always present in the matrix of polymer-derived ceramics due to the PA12 degradation [69, 70]. Fig. 4B shows the SiC ceramic structures generated after the conversion. Despite the high linear shrinking of about 21–25 %, the parts kept their designed shape for all the preceramics used. No macrocracks

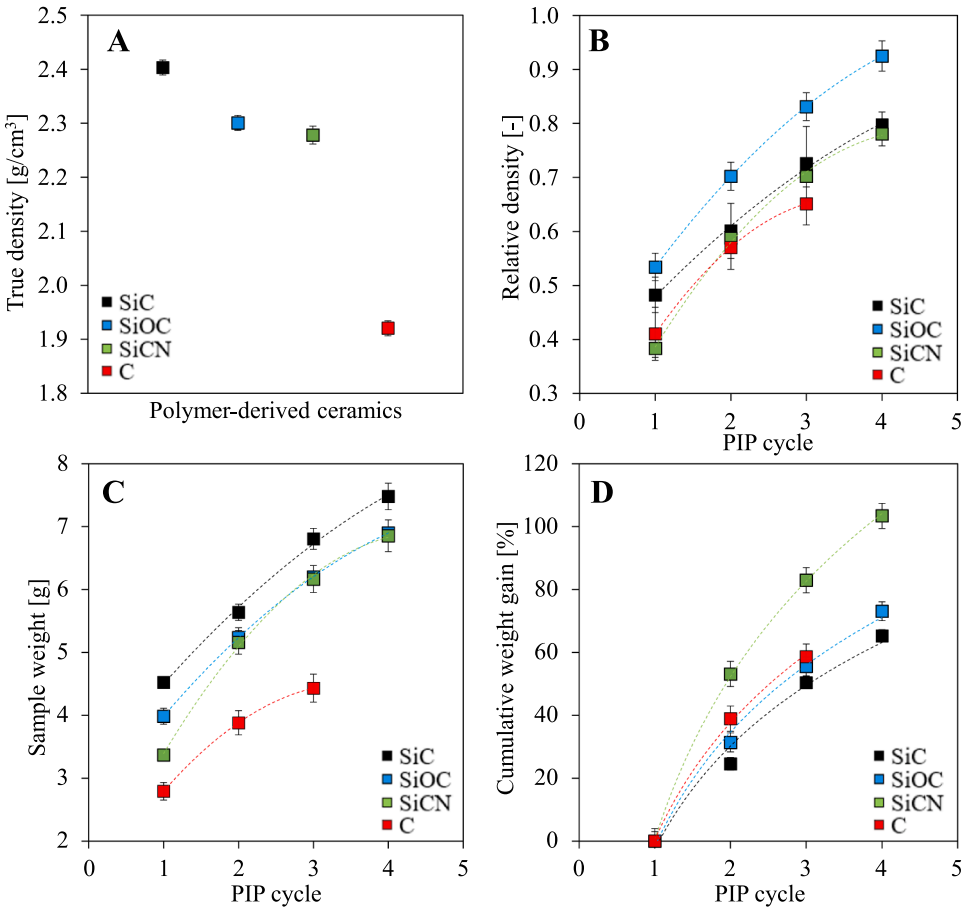

Fig. 5. Measurements on the produced polymer-derived ceramic samples: (A) true density; (B) relative density, (C) sample weight and cumulative weight gain (D) as a function of the PIP cycle.

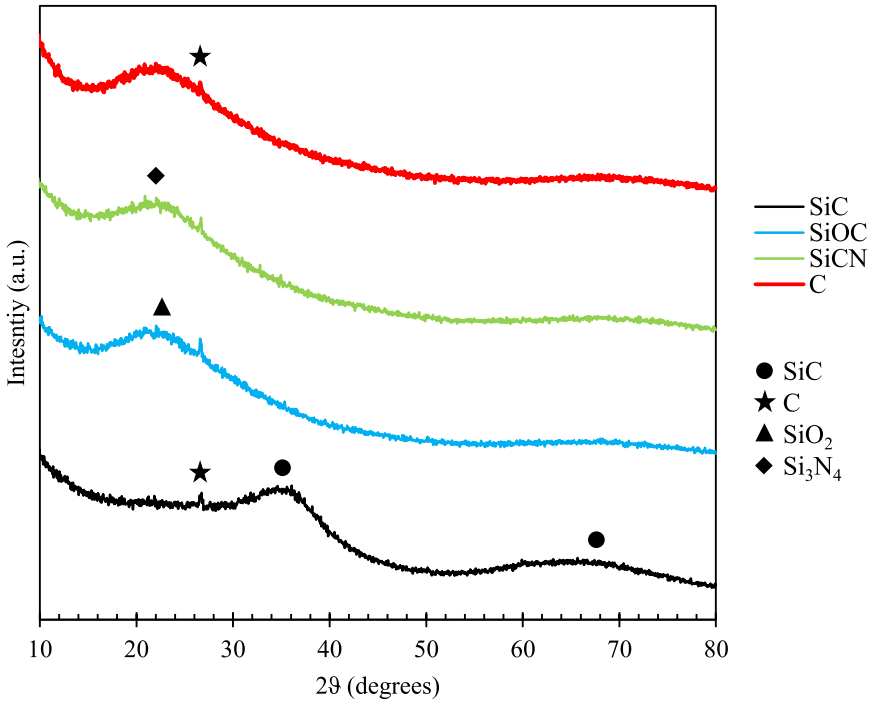

Fig. 6. XRD analysis of the polymer-derived ceramic architectures: SiC (black curve), SiOC (blue curve), SiCN (green curve) and C (red curve).

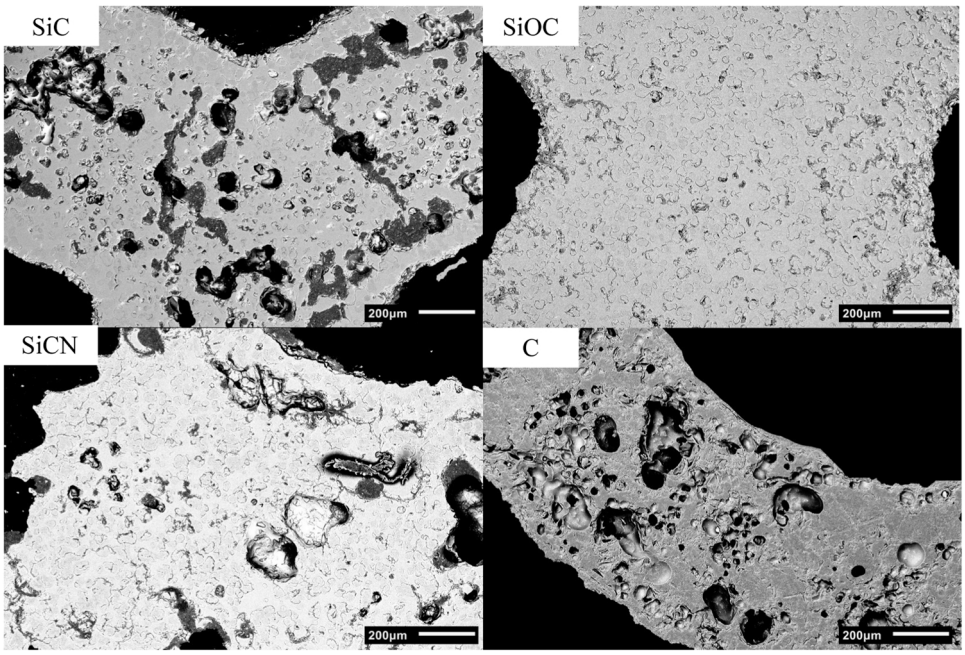

Fig. 7. SEM micrographs of the fracture surface of the produced polymer-derived ceramics samples.

or shape distortion were observed. No optical differences were observed between the SiC, SiOC and SiCN ceramics, and all had a dull black color (Fig. 4B and C), while the C structures showed instead a shiny grey color (Fig. 4D). The size of the samples was almost the same, while the mass was different, both after the conversion and after the various densification cycles.

Fig. 5 shows the measurements performed on the produced ceramic parts after each PIP cycle. The true density, apparent density and relative density were measured by helium pycnometry. The measured true densities (Fig. 5A) were in accordance with the values found in literatures for the same amorphous ceramics [44,45,75,76]. After the first conversion, the relative density of the ceramics was different due to: (i) the different infiltration rate, which depends on the wettability of the liquid preceramic polymers on the PA12 surface and (ii) their different ceramic yields. Also, the subsequent infiltrations resulted in a different relative density increase for the same reasons. The linear shrinkage developed only in the first conversion, as expected, leading to the production of cylindrical ceramic samples with ∼19 mm diameter and ∼34 mm height. The struts diameter and surfaces thickness shrunk accordingly. In subsequent PIP cycles, no shrinking was observed, and the structures maintained their shape and size.

Fig. 5B–D shows the comparison of the relative density, sample weight and cumulative weight gain after each PIP cycle. These charts offered an important comparison with the yield of the preceramic polymers presented in Fig. 3. At the first conversion, the SiCN had the lowest relative density (0.384) despite the yield of PSN alone being the highest (87 %). This means that probably the infiltration of the PA12 preform with PSN was not efficient due to not good wettability. However, in the subsequent cycles, the SiCN achieved the highest increase in terms of relative density (+50 %) and mass (+103 %), according to its yield, indicating that PSN had a good wettability on the SiCN surface. After the first conversion, the SiOC sample reached the highest relative density (0.534) due to the high yield of the PCSO (85 %) and probably to its good wettability with the PA12 surface. After 4 PIP cycles, the increase of relative density and mass were of 42 % and 73 % respectively. SiOC reached the highest relative density of 0.925. SiC showed a similar behavior to SiOC but with a lower yield. As expected, C showed in general the lowest yield.

Table 3
Mercury intrusion porosimetry analysis of the produced polymer-derived ceramics samples: interparticle, intraparticle and total porosity.

		SiC	SiOC	SiCN	C
Total porosity	%	20.2	7.4	22.0	34.8

3.3. Phase assemblage

Fig. 6 shows the results obtained on the SiC (black curve), SiOC (blue curve), SiCN (green curve) and C (red curve) ceramic samples. The analysis of the phases present was difficult due to the absence of crystallinity; indeed, the materials were all totally amorphous. All the measurements agreed with the trends reported in the literature. The phase assemblage of the SiC ceramics (black curve) was comprised by totally amorphous SiC and a very limited amount of graphitic carbon. The phase assemblage of SiOC comprised amorphous carbon and SiO_2. The curve for SiCN was in agreement with the Si_3N_4 record and showed a slight amount of carbon. C showed the presence of amorphous carbon. Negligible traces of SiO_2 were found in all the ceramics, which can correspond to the SiOC peak (according to literature [75]) produced with the first pyrolysis [69,70].

3.4. Microstructure

Fig. 7 shows the micrographs of the different ceramics. Black/dark grey areas are the pores of the materials. The light grey area is the ceramic phase. The SiC ceramics showed high compactness but also a high level of microporosity (Table 3 summarizes the porosity results). Several cracks were observed in the material and pores in the range of 10–100 µm can be detected. The SiOC ceramics after 4 PIP cycles had the highest level of compactness, with an almost fully dense solid phase. The microporosity in the materials was very low with pores of size < 10 µm. The SiCN as well as the SiC samples possessed high porosity. In this case larger pores were occasionally observed in the microstructure. The glassy carbon showed the highest level of porosity, with pores larger than 100 µm. The microstructure was also characterized by the presence of smaller pores (< 10 µm).

The mercury intrusion porosimetry analyses confirmed the SEM

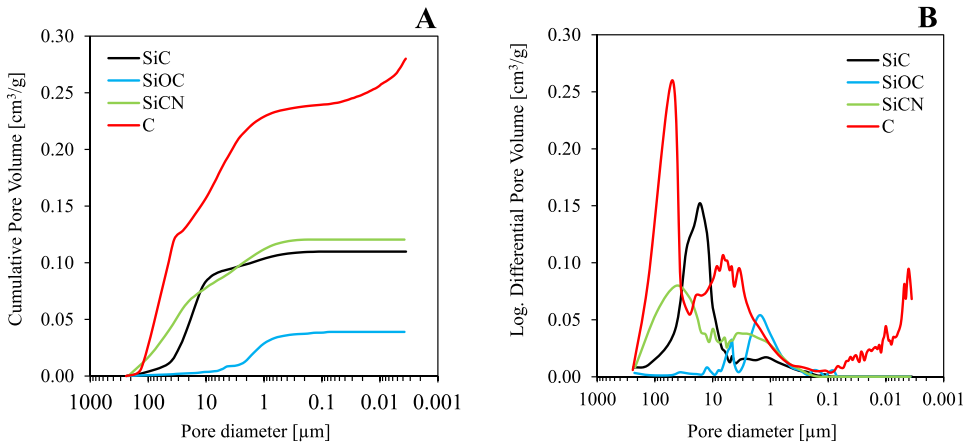

Fig. 8. Mercury intrusion porosimetry analysis of the produced polymer-derived ceramics samples: (A) cumulative pore volume and (B) log differential pore volume as a function of the pore diameter.

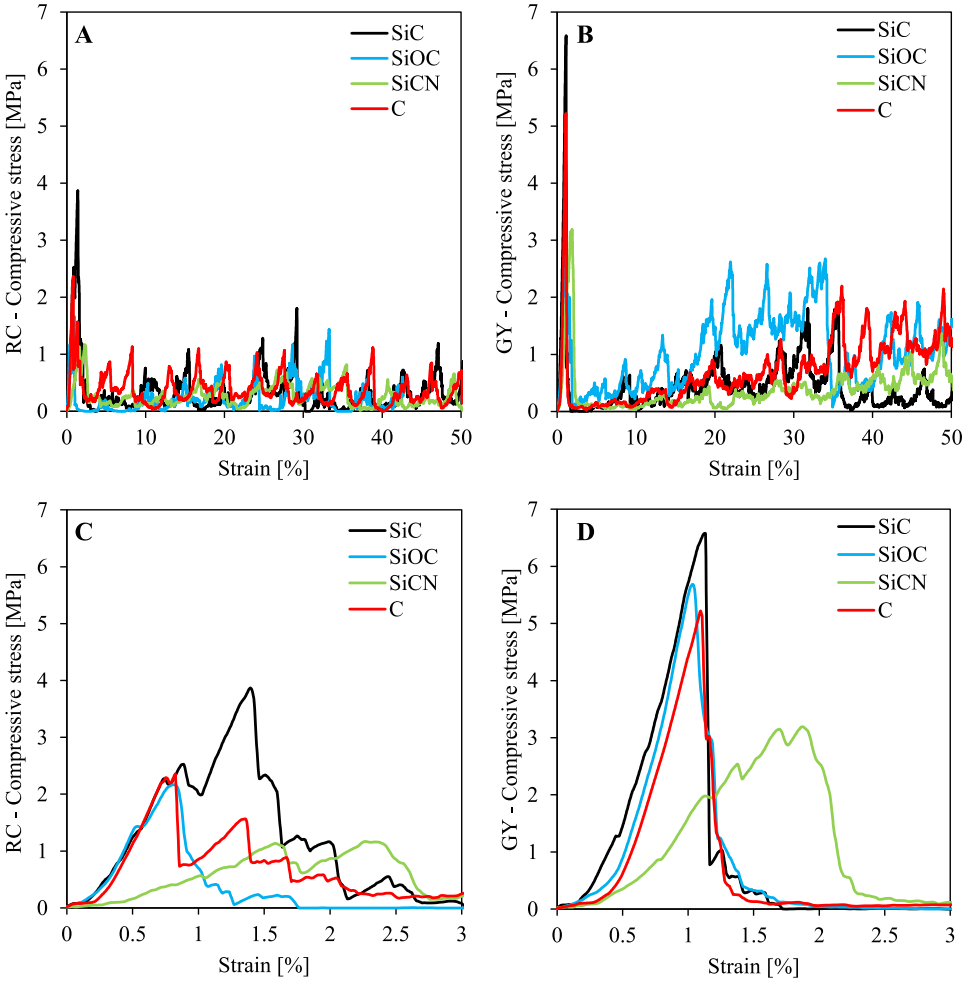

Fig. 9. Mechanical compression tests results of the produced SiC, SiOC, SiCN and C samples. (A-B) Stress-strain curves up to 50 % deformation, and (C-D) stress-strain curves with a magnification up to 3 % deformation for the RC and GY structure, respectively.

results. The SiC ceramics (black curve) contained a prevalence of pores in the range of 100–10 μm. The high slope in Fig. 8A and the high peak in Fig. 8B showed a large prevalence of 20 μm pores, which corresponds to an interparticle porosity of 17.4 %. The SiOC ceramics (blue curve) possessed a bimodal microstructure with several 5 μm pores and a prevalence of smaller pores in the range of 2–0.5 μm. The SiCN ceramics (green curve) had pores in the range of 200–1 μm. A large prevalence of 50 μm pores corresponds to an interparticle porosity of 16.4 %, and the total porosity was 21.9 %. The glassy carbon after three PIP (red curve) was comprised by a three-modal structure, with large pores between 200 and 30 μm (peak at 60 μm), medium pores between 30 and 0.5 μm (peak at 6 μm) and small pores between 0.1 and 0.004 μm (peak at 0.005 μm).

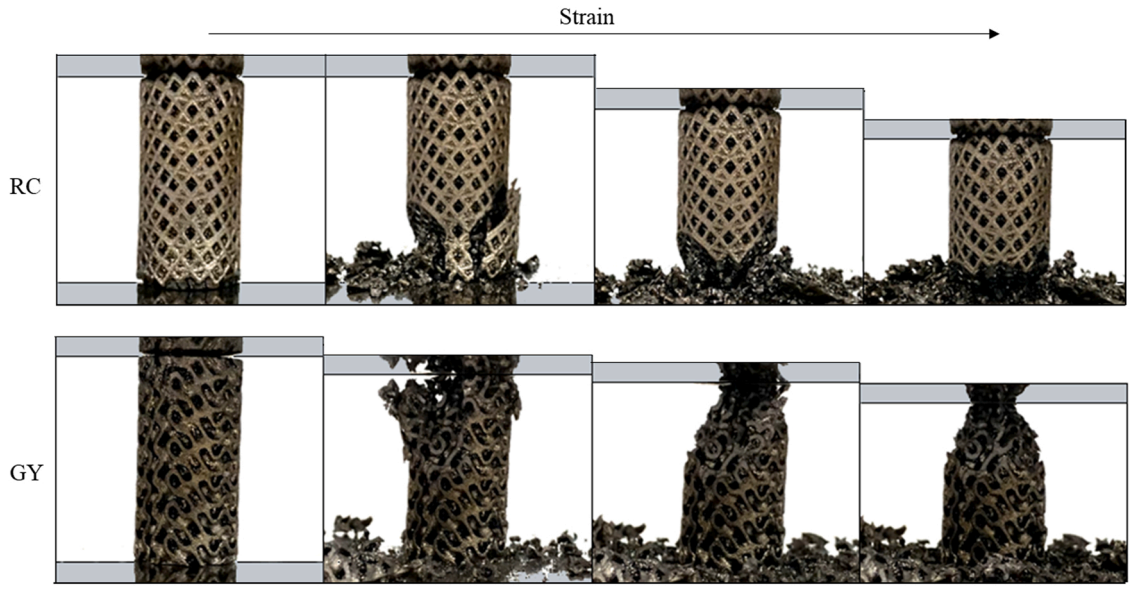

Fig. 10. Optical views during the compression tests at increasing strain rate of the polymer-derived SiC ceramics of the RC and GY architectures.

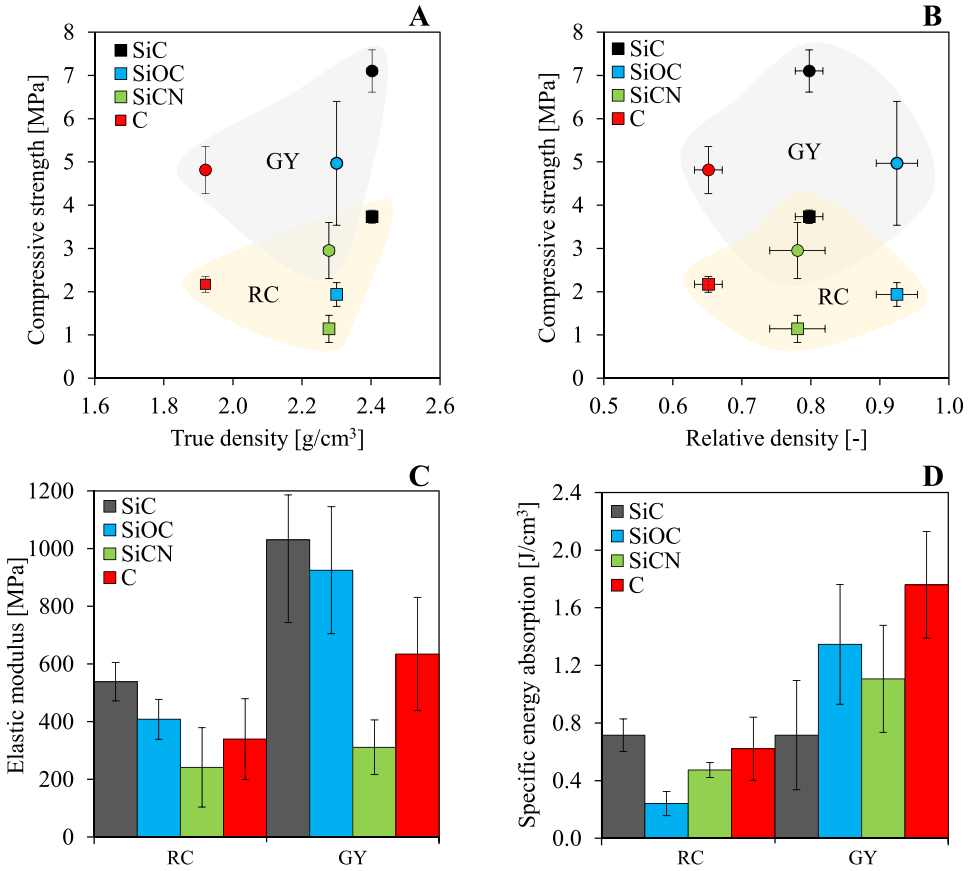

Fig. 11. Mechanical compression test results for the produced SiC, SiOC, SiCN and C samples. (A-B) Maximum compressive strength against the true density and the relative density. (C-D) Estimated elastic modulus and specific energy absorption for the different materials and architectures.

Furan resin was the only preceramic polymer used in this work which produced a structure containing nanopores. Table 3 summarizes the porosity results for the four types of ceramic samples produced.

3.5. Mechanical properties

Fig. 9 shows the resulting stress-strain curves of the four materials according to the two types of architecture. The trend typical of cellular structures under compression was observed. Both RC and GY are bending-dominated structures [77–79]. Fig. 9A and B show that the

Table 4
Comprehensive data of the compression tests results for the SiC, SiOC, SiCN and C samples.

Arch. [dimensionless]	Material [dimensionless]	Maximum load [N]	Compressive strength [MPa]	Elastic modulus [MPa]	Specific energy absorption (ε = 50 %) [J/cm^3]
RC	SiC	953 ± 281	3.7 ± 0.2	538 ± 66	0.716 ± 0.113
	SiOC	551 ± 76	1.9 ± 0.3	408 ± 69	0.241 ± 0.084
	SiCN	360 ± 92	1.1 ± 0.3	241 ± 138	0.474 ± 0.052
	C	621 ± 38	2.2 ± 0.2	340 ± 140	0.621 ± 0.219
GY	SiC	1924 ± 321	7.1 ± 0.5	1031 ± 156	0.716 ± 0.380
	SiOC	1361 ± 356	5.0 ± 1.4	925 ± 220	1.346 ± 0.415
	SiCN	932 ± 216	3.0 ± 0.6	311 ± 95	1.106 ± 0.372
	C	1378 ± 152	4.8 ± 0.5	635 ± 197	1.759 ± 0.369

stress-strain curves for the RC and GY had a similar trend but with different magnitude. Both structures showed the fragile behavior typical of ceramics. At the very beginning of the tests (see higher magnification in Fig. 9C and -D), the maximum stress was reached for all the ceramics at a strain between 0.8 % and 2.4 %. The SiCN ceramics reached the maximum stress with a higher deformation than the other ceramics. In general, once the first major crack in the architecture was created, it propagated into the various cells of the lattice leading to a stepwise behavior. This means that once the material fractured with the maximum force, it did not collapse but continued to support the load thanks to its cellular structure. This can be seen from the continuous compressive stress that was sustained up to 50 % deformation. Considering that between RC and GY of the same material there was no difference in terms of relative density, this allowed to directly compare the two geometries. In general, the geometry of the gyroid supported about twice as much load as the rotated cube. Furthermore, at large deformations (>20 %) the GY structure offered greater strength, thus leading to a lower propagation of cracks than for the RC one. Fig. 10 helps to understand the fracture behavior of the different architectures. The RC lattice after the first fracture (45° oriented) continued to fragment with a crack propagation at an almost constant rate, cell after cell. The crack propagated in the direction of the struts. Instead, the GY after the first fracture (also in this case 45° oriented) continued to support the load and proceeded with a slower crack propagation. In both cases, the collapse of the structure occurred by propagation of the initial crack through the cells of the structure, and indeed the cells remained intact in the opposite side of the fractured part.

Fig. 11A and B show the comparison of the produced materials and structures in terms of maximum compressive strength against their true density and relative density. Results showed that there is not a direct relation between the compressive strength with the true density and relative density. This means that the quality and type of the produced phase played the main role in the mechanical performances. The principal example is the glassy carbon, which were produced with one PIP cycle less than the other samples. It had a 17 % lower true density and 30 % lower relative density than SiOC, but it possessed about the same compressive strength for both architectures. The glassy carbon samples had also a 50 % and 38 % higher strength with respect to the SiCN ones for the RC and GY, respectively. The SiC ceramics had the highest strength of 3.7 ± 0.2 MPa and 7.1 ± 0.5 MPa for the RC and GY, respectively. In general, the samples with the GY architecture showed a higher compression strength than the RC ones, due to the presence of a continuous surface which is structurally less fragile, and better supports the load with respect to thin struts.

Fig. 11C shows the estimation of the elastic modulus for the produced ceramics and architectures. The calculation of the elastic modulus for ceramic materials is very complex due to the difficult measurement of their strain. For this reason, the data shown are an estimation and are useful only to compare the structures. The calculation is based on the slope of the stress-strain curve before the break, by taking two stress-strain points, the modulus is the change in stress divided by the change in strain. The large error bars can be attributed to the random cracking of the lattice cells. The values of the elastic modulus had, to a great extent, a similar trend as that of the strength plot. In general, the modulus of the GY structures was double that of RC, except for the SiCN ceramics which were similar. Considering that the relative density was the same for the two architectures of the same ceramics, the results means that the geometry of the lattice played an important role on the mechanical performance. The trend showed that the SiC ceramics had the highest value of 538 MPa and 1031 MPa for the RC and GY, respectively. The SiCN showed the lowest values.

Fig. 11D shows the specific energy absorption of the different materials and architectures. The calculation of the integral in the stress-strain curve was performed up to 50 % of the strain. The large error bars can be attributed to the random cracking of the lattice cells, and this behavior is more evident for the GY structures. As expected, in general the GY structure absorbed higher energy with respect to the RC of the same materials, in accordance with strength and modulus, except for the SiC architectures which absorbed the same energy, meaning that for this ceramic there was no influence of the geometry on the energy absorption (at the same relative density). The SiOC ceramics had the most significant influence of the architecture on the energy absorbed, with 550 % times increase from RC to GY. The maximum specific energy of 1.759 J/cm^3 was absorbed by the glassy carbon gyroid, because of its nanoporous structure (pores acted as a block for the crack propagation).

Table 4 summarizes the data of the compression tests of the polymer-derived ceramic samples.

4. Conclusions

A noteworthy advantage of the proposed method is the possibility of manufacturing net-shape ceramics directly from the preceramic precursor, without the need of using ceramic powders. Moreover, another benefit of this approach is that it is based an AM technology, powder bed fusion of thermoplastic powders, which has a much higher degree of maturity and lower cost with respect of processing of ceramic powders.

In this study, polycarbosilane (AHPCS), polycarbosiloxane (PCSO), polysilazane (PSN) and furan (FUR) polymers were used for the fabrication of the polymer-derived ceramics based on SiC, SiOC, SiCN and C respectively. Despite the high linear shrinking of about 21–25 %, the parts kept their designed shape for all the preceramic polymers used. At the first conversion, the SiCN samples had the lowest relative density (38.4 %) despite the yield of PSN alone was the highest (87 %), meaning that the infiltration of the PA12 preform with PSN was not efficient due to not good wettability. However, in the subsequent cycles, the SiCN samples achieved the highest increase in terms of relative density (+50 %) and mass (+103 %), according to its yield, indicating that PSN had good wettability on the SiCN surface. After the first conversion, SiOC reached the highest relative density (53.4 %) due to the high yield of the PCSO (85 %) and to its good wettability with the PA12 surface. After four PIP, SiOC reached the highest relative density of 92.5 %. SiC architectures showed the higher strength of 3.7 ± 0.2 MPa and 7.1 ± 0.5 MPa for the RC and GY, respectively.

Declaration of Competing Interest

The authors declare that they have no known competing financial interests or personal relationships that could have appeared to influence the work reported in this paper.

References

[1] M. Belmonte, Advanced ceramic materials for high temperature applications, Adv. Eng. Mater. 8 (8) (2006) 693–703, https://doi.org/10.1002/adem.200500269.
[2] W. Krenkel, Ceramic Matrix Composites: Fiber Reinforced Ceramics and Their Applications, John Wiley\& Sons, 2008.
[3] T.O. Mason, Advanced Ceramics, Encyclopedia Britannica, 2016. ⟨https://www.britannica.com/technology/advanced-ceramics⟩.
[4] O. Santoliquido, et al., Structured alumina substrates for environmental catalysis produced by stereolithography, Appl. Sci. 11 (17) (2021), https://doi.org/10.3390/app11178239.
[5] M. Pelanconi, M. Barbato, S. Zavattoni, G.L. Vignoles, A. Ortona, Thermal design, optimization and additive manufacturing of ceramic regular structures to maximize the radiative heat transfer, Mater. Des. 163 (2019), https://doi.org/10.1016/j.matdes.2018.107539.
[6] O. Al-Ketan, M. Pelanconi, A. Ortona, R.K. Abu Al-Rub, Additive manufacturing of architected catalytic ceramic substrates based on triply periodic minimal surfaces, J. Am. Ceram. Soc. 102 (10) (2019) 6176–6193, https://doi.org/10.1111/jace.16474.
[7] M. Pelanconi, et al., Application of ceramic lattice structures to design compact, high temperature heat exchangers: material and architecture selection, Materials 14 (12) (2021), https://doi.org/10.3390/ma14123225.
[8] A. Sommers, Q. Wang, X. Han, C. T'Joen, Y. Park, A. Jacobi, Ceramics and ceramic matrix composites for heat exchangers in advanced thermal systems-A review, Appl. Therm. Eng. 30 (11–12) (2010) 1277–1291, https://doi.org/10.1016/j.applthermaleng.2010.02.018.
[9] Z. Chen, et al., 3D printing of ceramics: a review, J. Eur. Ceram. Soc. 39 (4) (2019) 661–687, https://doi.org/10.1016/j.jeurceramsoc.2018.11.013.
[10] N. Travitzky, et al., Additive manufacturing of ceramic-based materials, Adv. Eng. Mater. 16 (6) (2014) 729–754, https://doi.org/10.1002/adem.201400097.
[11] T. Chartier, et al., Additive manufacturing to produce complex 3D ceramic parts, J. Ceram. Sci. Technol. 6 (2) (2015) 95–104, https://doi.org/10.4416/JCST2014-00040.
[12] A. Zocca, P. Colombo, C.M. Gomes, J. Günster, Additive manufacturing of ceramics: issues, potentialities, and opportunities, J. Am. Ceram. Soc. 98 (7) (2015) 1983–2001, https://doi.org/10.1111/jace.13700.
[13] T. Moritz, S. Maleksaeedi, in: J. Zhang, Y.-G.B.T.-A.M. Jung (Eds.), 4 - Additive Manufacturing of Ceramic Components, Butterworth-Heinemann, 2018, pp. 105–161, https://doi.org/10.1016/B978-0-12-812155-9.00004-9.
[14] Z. Lu, J. Cao, Z. Song, D. Li, B. Lu, Research progress of ceramic matrix composite parts based on additive manufacturing technology, Virtual Phys. Prototyp. 14 (4) (2019) 333–348, https://doi.org/10.1080/17452759.2019.1607759.
[15] M.R. O'Masta, E. Stonkevitch, K.A. Porter, P.P. Bui, Z.C. Eckel, T.A. Schaedler, Additive manufacturing of polymer-derived ceramic matrix composites, J. Am. Ceram. Soc. 103 (12) (2020) 6712–6723, https://doi.org/10.1111/jace.17275.
[16] W. Wang, et al., Additive manufacturing of fiber reinforced ceramic matrix composites: Advances, challenges, and prospects, Ceram. Int. 48 (14) (2022) 19542–19556, https://doi.org/10.1016/j.ceramint.2022.04.146.
[17] J. Sun, et al., A review on additive manufacturing of ceramic matrix composites, J. Mater. Sci. Technol. (2022), https://doi.org/10.1016/j.jmst.2022.06.039.
[18] L. Schlier, W. Zhang, N. Travitzky, P. Greil, J. Cypris, M. Weclas, Macro-cellular silicon carbide reactors for nonstationary combustion under piston engine-like conditions, Int. J. Appl. Ceram. Technol. 8 (5) (2011) 1237–1245, https://doi.org/10.1111/j.1744-7402.2010.02591.x.
[19] U. Scheithauer, E. Schwarzer, T. Moritz, A. Michaelis, Additive manufacturing of ceramic heat exchanger: opportunities and limits of the lithography-based ceramic manufacturing (LCM), J. Mater. Eng. Perform. 27 (1) (2018) 14–20, https://doi.org/10.1007/s11665-017-2843-z.
[20] O.H. Laguna, P.F. Lietor, F.J.I. Godino, F.A. Corpas-Iglesias, A review on additive manufacturing and materials for catalytic applications: milestones, key concepts, advances and perspectives, Mater. Des. 208 (2021), 109927, https://doi.org/10.1016/j.matdes.2021.109927.
[21] C.L. Cramer, et al., Additive Manufacturing of Ceramic Materials for Energy Applications: Road Map and Opportunities, 42, Elsevier Ltd, 2022, https://doi.org/10.1016/j.jeurceramsoc.2022.01.058.
[22] J. Zhu, et al., Recent advances in 3D printing for catalytic applications, Chem. Eng. J. 433 (P1) (2022), 134341, https://doi.org/10.1016/j.cej.2021.134341.
[23] T. Koyanagi, K. Terrani, S. Harrison, J. Liu, Y. Katoh, Additive manufacturing of silicon carbide for nuclear applications, J. Nucl. Mater. 543 (2021), 152577, https://doi.org/10.1016/j.jnucmat.2020.152577.
[24] J.W. Halloran, Ceramic stereolithography: additive manufacturing for ceramics by photopolymerization, Annu. Rev. Mater. Res. 46 (2016) 19–40, https://doi.org/10.1146/annurev-matsci-070115-031841.
[25] K. Shahzad, J. Deckers, J.P. Kruth, J. Vleugels, Additive manufacturing of alumina parts by indirect selective laser sintering and post processing, J. Mater. Process. Technol. 213 (9) (2013) 1484–1494, https://doi.org/10.1016/j.jmatprotec.2013.03.014.
[26] L. Rueschhoff, W. Costakis, M. Michie, J. Youngblood, R. Trice, Additive manufacturing of dense ceramic parts via direct ink writing of aqueous alumina suspensions, Int. J. Appl. Ceram. Technol. 13 (5) (2016) 821–830, https://doi.org/10.1111/ijac.12557.
[27] M. Schwentenwein, J. Homa, Additive manufacturing of dense alumina ceramics, Int. J. Appl. Ceram. Technol. 12 (1) (2015) 1–7, https://doi.org/10.1111/ijac.12319.
[28] H. Wu, et al., Fabrication of dense zirconia-toughened alumina ceramics through a stereolithography-based additive manufacturing, Ceram. Int. 43 (1, Part B) (2017) 968–972, https://doi.org/10.1016/j.ceramint.2016.10.027.
[29] R. Melcher, S. Martins, N. Travitzky, P. Greil, Fabrication of Al2O3-based composites by indirect 3D-printing, Mater. Lett. 60 (4) (2006) 572–575, https://doi.org/10.1016/j.matlet.2005.09.059.
[30] J. Barberi, et al., Robocasting of SiO2-based bioactive glass scaffolds with porosity gradient for bone regeneration and potential load-bearing applications, Materials 12 (17) (2019), https://doi.org/10.3390/ma12172691.
[31] A. Gómez-Gómez, J.J. Moyano, B. Román-Manso, M. Belmonte, P. Miranzo, M. I. Osendi, Highly-porous hierarchical SiC structures obtained by filament printing and partial sintering, J. Eur. Ceram. Soc. 39 (4) (2019) 688–695, https://doi.org/10.1016/j.jeurceramsoc.2018.12.034.
[32] W. Du, M. Singh, D. Singh, Binder jetting additive manufacturing of silicon carbide ceramics: development of bimodal powder feedstocks by modeling and experimental methods, Ceram. Int. 46 (12) (2020) 19701–19707, https://doi.org/10.1016/j.ceramint.2020.04.098.
[33] R. Liu, et al., Fabrication of porous SiC by direct selective laser sintering effect of boron carbide, Metals 11 (5) (2021) 737, https://doi.org/10.3390/met11050737.
[34] P. Delhaes, Chemical vapor deposition and infiltration processes of carbon materials, Carbon N.Y. 40 (5) (2002) 641–657, https://doi.org/10.1016/S0008-6223(01)00195-6.
[35] D.P. Stinton, A.J. Caputo, R.A. Lowden, Synthesis of fiber-reinforced SiC composites by chemical vapor infiltration, Am. Ceram. Soc. Bull. 65 (2) (1986) 347–350.
[36] L. Macdonald, Facile fabrication of SiC matrix composites using novel preceramic polymers, Adv. Sci./Sci. Ceram. Compos.: Dev. Appl. Energy Syst. (2006) 87–95, https://doi.org/10.1002/9781118406014.ch7.
[37] S.M. Dong, Y. Katoh, A. Kohyama, S.T. Schwab, L.L. Snead, Microstructural evolution and mechanical performances of SiC/SiC composites by polymer impregnation/microwave pyrolysis (PIMP) process, Ceram. Int. 28 (8) (2002) 899–905, https://doi.org/10.1016/S0272-8842(02)00071-8.
[38] M. Kotani, A. Kohyama, K. Okamura, T. Inoue, Fabrication of high performance SiC/SiC composite by polymer impregnation and pyrolysis method, in: Proceedings of the 23rd Annual Conference on Composites, Advanced Ceramics, Materials, and Structures: B: Ceramic Engineering and Science Proceedings. pp. 309–316, Jan. 01, 1999. ⟨https://doi.org/10.1002/9780470294574.ch36⟩.
[39] R. Sreeja, B. Swaminathan, A. Painuly, T.V. Sebastian, S. Packirisamy, Allylhydridopolycarbosilane (AHPCS) as matrix resin for C/SiC ceramic matrix composites, Mater. Sci. Eng. B Solid-State Mater. Adv. Technol. 168 (1) (2010) 204–207, https://doi.org/10.1016/j.mseb.2009.12.033.
[40] P. Sangsuwan, J.A. Orejas, J.E. Gatica, S.N. Tewari, M. Singh, Reaction-bonded silicon carbide by reactive infiltration, Ind. Eng. Chem. Res. 40 (23) (2001) 5191–5198, https://doi.org/10.1021/ie001029e.
[41] J.M. Qian, J.P. Wang, Z.H. Jin, Preparation and properties of porous microcellular SiC ceramics by reactive infiltration of Si vapor into carbonized basswood, Mater. Chem. Phys. 82 (3) (2003) 648–653, https://doi.org/10.1016/S0254-0584(03)00330-4.
[42] Y. Wang, S. Tan, D. Jiang, The effect of porous carbon preform and the infiltration process on the properties of reaction-formed SiC, Carbon N.Y. 42 (8–9) (2004) 1833–1839, https://doi.org/10.1016/j.carbon.2004.03.018.
[43] J.M. Qian, Z.H. Jin, X.W. Wang, Porous SiC ceramics fabricated by reactive infiltration of gaseous silicon into charcoal, Ceram. Int. 30 (6) (2004) 947–951, https://doi.org/10.1016/j.ceramint.2003.11.001.
[44] P. Colombo, G. Mera, R. Riedel, G.D. Sorarù, Polymer-derived ceramics: 40 Years of research and innovation in advanced ceramics, J. Am. Ceram. Soc. 93 (7) (2010) 1805–1837, https://doi.org/10.1111/j.1551-2916.2010.03876.x.
[45] C. Vakifahmetoglu, D. Zeydanli, P. Colombo, Porous polymer derived ceramics, Mater. Sci. Eng. R. Rep. 106 (2016) 1–30, https://doi.org/10.1016/j.mser.2016.05.001.
[46] P. Colombo, J. Schmidt, G. Franchin, A. Zocca, J. Günster, Additive manufacturing techniques for fabricating complex ceramic components from preceramic polymers. By Paolo Colombo, Johanna Schmidt, Giorgia Franchin, Andrea Zocca, and Jens Günster. Retrieved from www.ceramics.orgbricatin, [Online]. Available: www.ceramics.org.
[47] G. Franchin, et al., Additive manufacturing of ceramics from liquid feedstocks, Chin. J. Mech. Eng. Addit. Manuf. Front. 1 (1) (2022), 100012, https://doi.org/10.1016/j.cjmeam.2022.100012.
[48] R.P. Chaudhary, et al., Additive manufacturing of polymer-derived ceramics: materials, technologies, properties and potential applications, Prog. Mater. Sci. 128 (2022), 100969, https://doi.org/10.1016/j.pmatsci.2022.100969.
[49] G. Ding, R. He, K. Zhang, N. Zhou, H. Xu, Stereolithography 3D printing of SiC ceramic with potential for lightweight optical mirror, Ceram. Int. 46 (11) (2020) 18785–18790, https://doi.org/10.1016/j.ceramint.2020.04.196.
[50] E. Zanchetta, et al., Stereolithography of SiOC ceramic microcomponents, Adv. Mater. 28 (2) (2016) 370–376, https://doi.org/10.1002/adma.201503470.
[51] X. Wang, F. Schmidt, D. Hanaor, P.H. Kamm, S. Li, A. Gurlo, Additive manufacturing of ceramics from preceramic polymers: a versatile

stereolithographic approach assisted by thiol-ene click chemistry, Addit. Manuf. 27 (2019) 80–90, https://doi.org/10.1016/j.addma.2019.02.012.
[52] J. Schmidt, P. Colombo, Digital light processing of ceramic components from polysiloxanes, J. Eur. Ceram. Soc. 38 (1) (2018) 57–66, https://doi.org/10.1016/j.jeurceramsoc.2017.07.033.
[53] Y. de Hazan, D. Penner, SiC and SiOC ceramic articles produced by stereolithography of acrylate modified polycarbosilane systems, J. Eur. Ceram. Soc. 37 (16) (2017) 5205–5212, https://doi.org/10.1016/j.jeurceramsoc.2017.03.021.
[54] J. Tang, H. Chang, X. Guo, M. Liu, Y. Wei, Preparation of photosensitive SiO 2 / SiC ceramic slurry with high solid content for stereolithography, Ceram. Int. (2022), https://doi.org/10.1016/j.ceramint.2022.06.306.
[55] G. Pierin, C. Grotta, P. Colombo, C. Mattevi, Direct Ink Writing of micrometric SiOC ceramic structures using a preceramic polymer, J. Eur. Ceram. Soc. 36 (7) (2016) 1589–1594, https://doi.org/10.1016/j.jeurceramsoc.2016.01.047.
[56] K. Huang, H. Elsayed, G. Franchin, P. Colombo, Additive manufacturing of SiOC scaffolds with tunable structure-performance relationship, J. Eur. Ceram. Soc. 41 (15) (2021) 7552–7559, https://doi.org/10.1016/j.jeurceramsoc.2021.08.043.
[57] H. Xiong, et al., Building SiC-based composites from polycarbosilane-derived 3D-SiC scaffolds via polymer impregnation and pyrolysis (PIP), J. Eur. Ceram. Soc. 41 (2) (2021) 1121–1131, https://doi.org/10.1016/j.jeurceramsoc.2020.09.059.
[58] Y. Yang, A. Kulkarni, G.D. Soraru, J.M. Pearce, A. Motta, 3d printed sioc(N) ceramic scaffolds for bone tissue regeneration: improved osteogenic differentiation of human bone marrow-derived mesenchymal stem cells, Int. J. Mol. Sci. 22 (24) (2021), https://doi.org/10.3390/ijms222413676.
[59] A. Kulkarni, G.D. Sorarù, J.M. Pearce, Polymer-derived SiOC replica of material extrusion-based 3-D printed plastics, Addit. Manuf. 32 (2020), 100988, https://doi.org/10.1016/j.addma.2019.100988.
[60] A. Kulkarni, J. Pearce, Y. Yang, A. Motta, G.D. Sorarù, SiOC(N) cellular structures with dense struts by integrating fused filament fabrication 3D printing with polymer-derived ceramics, Adv. Eng. Mater. 23 (12) (2021), https://doi.org/10.1002/adem.202100535.
[61] C.L. Cramer, et al., Processing and properties of SiC composites made via binder jet 3D printing and infiltration and pyrolysis of preceramic polymer, Int. J. Ceram. Eng. Sci. 2 (6) (2020) 320–331, https://doi.org/10.1002/ces2.10070.
[62] A. Baux, et al., Synthesis and properties of macroporous SiC ceramics synthesized by 3D printing and chemical vapor infiltration/deposition, J. Eur. Ceram. Soc. 40 (8) (2020) 2834–2854, https://doi.org/10.1016/j.jeurceramsoc.2020.03.001.
[63] C. Heisel, C. Caliot, T. Chartier, S. Chupin, P. David, D. Rochais, Digital design and 3D printing of innovative SiC architectures for high temperature volumetric solar receivers, Sol. Energy Mater. Sol. Cells 232 (2021), 111336, https://doi.org/10.1016/j.solmat.2021.111336.
[64] C.L. Cramer, et al., Properties of SiC-Si made via binder jet 3D printing of SiC powder, carbon addition, and silicon melt infiltration, J. Am. Ceram. Soc. 104 (11) (2021) 5467–5478, https://doi.org/10.1111/jace.17933.
[65] A. Fleisher, et al., Reaction bonding of silicon carbides by Binder Jet 3D-Printing, phenolic resin binder impregnation and capillary liquid silicon infiltration, Ceram. Int. 45 (14) (2019) 18023–18029.
[66] M. Pelanconi, E. Rezaei, A. Ortona, Cellular ceramic architectures produced by hybrid additive manufacturing: A review on the evolution of their design, J. Ceram. Soc. Jpn. 128 (9) (2020), https://doi.org/10.2109/jcersj2.20071.
[67] M. Pelanconi and A. Ortona, Review on the Design Approaches of Cellular Architectures Produced by Additive Manufacturing BT - Industrializing Additive Manufacturing, 2021, pp. 52–64.
[68] M. Pelanconi, A. Ortona, Nature-inspired, ultra-lightweight structures with gyroid cores produced by additive manufacturing and reinforced by unidirectional carbon fiber ribs, Materials 12 (24) (2019), https://doi.org/10.3390/ma1224134.
[69] M. Pelanconi, P. Colombo, A. Ortona, Additive manufacturing of silicon carbide by selective laser sintering of PA12 powders and polymer infiltration and pyrolysis, J. Eur. Ceram. Soc. 41 (10) (. 2021) 5056–5065, https://doi.org/10.1016/J.JEURCERAMSOC.2021.04.014.
[70] M. Pelanconi, G. Bianchi, P. Colombo, A. Ortona, Fabrication of dense SiSiC ceramics by a hybrid additive manufacturing process, J. Am. Ceram. Soc. 105 (2) (. 2022) 786–793, https://doi.org/10.1111/jace.18134.
[71] R. Anand, B.B. Nayak, S.K. Behera, Phase, nanostructure, and oxidation of precursor derived SiCN–TiO2 ceramic nanocomposites, Ceram. Int. 47 (19) (2021) 27822–27832.
[72] M.A. Schiavon, G.D. Soraru, I.V.P. Yoshida, Synthesis of a polycyclic silazane network and its evolution to silicon carbonitride glass, J. Non Cryst. Solids 304 (1–3) (2002) 76–83.
[73] P. Furtat, M. Lenz-Leite, E. Ionescu, R.A.F. Machado, G. Motz, Synthesis of fluorine-modified polysilazanes via Si–H bond activation and their application as protective hydrophobic coatings, J. Mater. Chem. A 5 (48) (2017) 25509–25521.
[74] B. Santhosh, C. Vakifahmetoglu, E. Ionescu, A. Reitz, B. Albert, G.D. Soraru, Processing and thermal characterization of polymer derived SiCN (O) and SiOC reticulated foams, Ceram. Int. 46 (5) (2020) 5594–5601.
[75] G.D. Sorarù, S. Modena, E. Guadagnino, P. Colombo, J. Egan, C. Pantano, Chemical durability of silicon oxycarbide glasses, J. Am. Ceram. Soc. 85 (6) (2002) 1529–1536.
[76] A. Zambotti, et al., Synthesis and thermal evolution of polysilazane-derived SiCN (O) aerogels with variable C content stable at 1600 °C, Ceram. Int. 47 (6) (2021) 8035–8043, https://doi.org/10.1016/j.ceramint.2020.11.157.
[77] A. Alghamdi, T. Maconachie, D. Downing, M. Brandt, M. Qian, M. Leary, Effect of additive manufactured lattice defects on mechanical properties: an automated method for the enhancement of lattice geometry, Int. J. Adv. Manuf. Technol. 108 (3) (2020) 957–971.
[78] T. Maconachie, et al., The compressive behaviour of ABS gyroid lattice structures manufactured by fused deposition modelling, Int. J. Adv. Manuf. Technol. 107 (11) (2020) 4449–4467.
[79] A. Parisien, M.S.A. ElSayed, H. Frei, Mechanoregulation modelling of stretching versus bending dominated periodic cellular solids, Mater. Today Commun. 33 (2022), 104315.